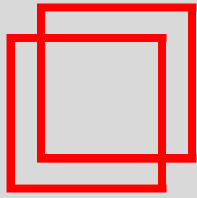

Math-Net.Ru
All Russian mathematical portal

A. V. Ankudinov, On the accuracy of the probe-sample contact stiffness measured by an atomic force microscope,
Nanosystems: Physics, Chemistry, Mathematics, 2019, Volume 10, Issue 6, 642–653

https://www.mathnet.ru/eng/nano480

Use of the all-Russian mathematical portal Math-Net.Ru implies that you have read and agreed to these terms of use
https://www.mathnet.ru/eng/agreement

Download details:
IP: 18.97.9.168
April 25, 2025, 01:31:26

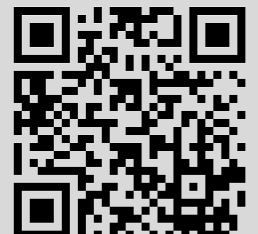

NANOSYSTEMS: PHYSICS, CHEMISTRY, MATHEMATICS, 2019, 10 (6), P. 642–653

On the accuracy of the probe-sample contact stiffness measured by an atomic force microscope

A. V. Ankudinov

Ioffe Institute, 26 Politekhnicheskaya, Saint-Petersburg 194021, Russia

Alexander.ankudinov@mail.ioffe.ru

PACS 07.79.Lh **DOI 10.17586/2220-8054-2019-10-6-642-653**

To improve the accuracy of atomic force microscopy in nanomechanical experiments, an analytical model is proposed to study the static interaction of a cantilever in contact with a sample. The model takes into account: the cantilever probe is clamped by the sample or slides along its surface, the geometric and mechanical characteristics of the sample and the cantilever, their relative orientation. The cantilever console bending and torsion angles as functions of the sample displacements in three orthogonal directions have been measured by atomic force microscopy with an optical beam deflection scheme.The measurements are in good agreement with the simulation.

Keywords: AFM, cantilever, sliding and clamping probesample contact.

Received: 28 October 2019

1. Introduction

In atomic force microscopy (AFM) [1], local mechanical properties of a sample are studied using load–unloading dependencies of the indentation force on the sample deformation, force curves. They play a special role in the novel techniques [2] based on the so-called jumping mode AFM [3,4]: PeakForce QNM (Bruker), HybriD mode (NT–MDT SI), Fast force mapping mode (Asylum Research). The force curves are used to determine the height of the relief and serve as the basis for electrical, piezoelectric, magnetic, and thermal measurements [5].

A significant instrumental contribution to the shape of the force curve can be made by the friction in the AFM probe–sample contact. If the cantilever probe (the probe) slides over the surface, the force applied to the probe tip acts perpendicular to the sample and bends the cantilever beam (the console) so that the bending angle grows monotonously along the console [6, 7]. If the probe is clamped on the sample, a significant lateral friction force is added. This force buckles the console (the buckling angle varies non-monotonously along the console) [6, 7]. In the AFM device with an optical beam deflection system (OBD) [8], the deflection angle is monitored on the console locally, at the focus point of the OBD laser beam. Since the angle profile along the console is unknown, the AFM control system is not able to distinguish between the bending and the buckling of the console [9, 10], which leads to errors of the measured amplitude and direction of the indentation force. In principle, the OBD detects two parameters (bending and torsion angles of the console at the selected point), but both the contact point displacement vector and the concentrated force have three spatial components. Only recently a commercially available scheme for monitoring console deflections has appeared [11], combining the OBD with an interferometer [12] that allows measuring the missing third parameter – the console vertical displacement at the selected point.

In AFM, the normal stiffness of the probe–sample contact k_S is calculated from S, the force curve slope at the point of interest on the sample, S_0, this slope at the conditionally infinitely rigid and flat sample, and the console bending stiffness k_C, [13]:

$$k_S = \frac{k_C S}{S_0 - S}. \tag{1}$$

The equation (1) directly stems from the model of two springs, describing the AFM probe–sample contact interaction, see Fig. 1. This model does not take into account the following factors: the probe is clamped or slides over the sample, the deformation of the probe itself, the local sample inclination and the possible anisotropy of sample's mechanical properties, design features and location of the cantilever above the sample. It is more correct to think that expression (1) calculates a conditional, apparent stiffness k_A, instead of the k_S. As a result, this simple model may turn out to be a source of unreliable results in nanomechanical studies using AFM.

This work offers an analytical model of the mechanical system console–probe–sample, accounting the above mentioned factors. To describe the equilibrium states of the system, the minimum of its mechanical energy is determined. We analyze the deformation redistribution between three subsystems: the console with the non-deformable probe – the "ideal cantilever"; the deformable probe; and the sample. In each subsystem, the stiffness tensor linearly couples the concentrated force vector applied to the probe tip (at the contact point) with the deformation vector. General solutions are obtained for two types of holonomic constraints: the probe is clamped on the sample; the probe slides along the

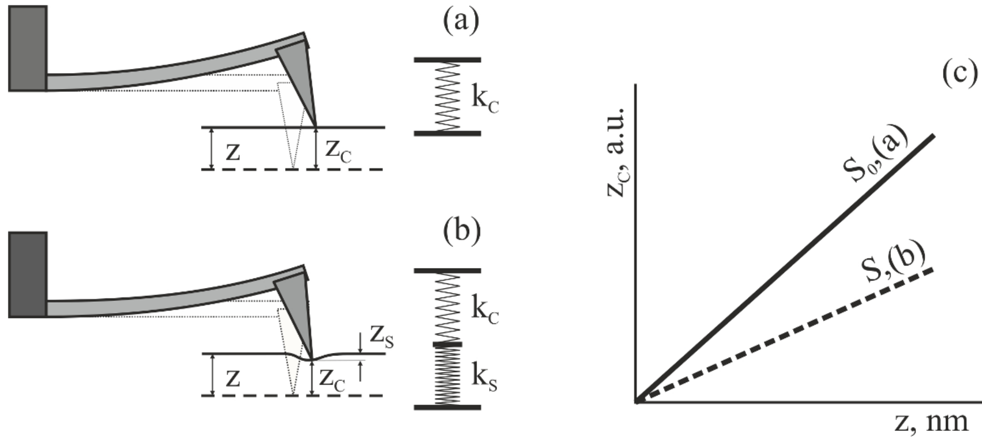

FIG. 1. Simple models of the AFM contact with a solid surface (a), with a soft sample (b). Cantilever and soft sample deformations are described using two springs: k_C and k_S. (c) Dependencies of the cantilever deviation Z^C on the sample vertical displacement Z: the solid sample, the calibration slope S_0,(a); the soft sample, the slope S,(b). Z^S on (b) denotes the sample deformation

sample selected plane. The contact of the so-called "real cantilever" (the console with the deform able probe) and the mechanically isotropic sample is examined in detail. Depending on the position of the OBD laser focus point on the console, the normalized sensitivities of its bending and torsion angles to the sample displacement along three orthogonal directions were calculated and as well measured. Good agreement between calculations and measurements is demonstrated.

2. Theoretical analysis

2.1. "Ideal cantilever"

First, consider the "ideal cantilever", that is, one in which the applied force deforms only the console, but not the probe, Fig. 2. Let the Y axis of the YZ coordinate system be directed along the rectangular console, and the coordinate origin is at the console attachment line to the chip, Fig. 2(a). The console displacement profile due to the force $\mathbf{F}$ acting in the YZ plane is expressed as follows [6]:

$$Z\left(Y,\mathbf{F}\right)=\left(2/E_C w t^3\right)\left\{3l_T Y^2 F_Y+\left(3l_C Y^2-Y^3\right)F_Z\right\},\tag{2}$$

where E_C is the Young's modulus of the console; w, t and l_C its width, thickness and length; l_T is the probe height. We introduce the parameters: $\lambda=l_T/l_C$, the console stiffness $k_C=E_C w t^3/4l_C^3$, the normalized coordinate $\psi=Y/l_C$, – and rewrite (2) in a more concise form:

$$Z\left(\psi,\mathbf{F}\right)=\left(1/2k_C\right)\left\{3\lambda\psi^2 F_Y+\left(3\psi^2-\psi^3\right)F_Z\right\}.\tag{2a}$$

The displacement profile (2a) corresponds to the profile of the bending angle of the console of the ideal cantilever:

$$\alpha\left(\psi,\mathbf{F}\right)=l_C^{-1}\cdot dZ\left(\psi\right)/d\psi=\left(3/2k_C l_C\right)\left\{2\lambda\psi F_Y+\left(2\psi-\psi^2\right)F_Z\right\}.\tag{2b}$$

In AFM the console bending is small and the angle $\alpha\left(\psi,\mathbf{F}\right)\ll 1$. Therefore, the vector $\mathbf{r^C}$ components of the "ideal cantilever", the probe tip displacements, are quite accurately related linearly with the displacement and the angle corresponding to the console end ($\psi=1$):

$$Z^C=Z\left(1,\mathbf{F}\right),\quad Y^C=l_T\alpha\left(1,\mathbf{F}\right).\tag{3}$$

Using (2a), (2b), (3) and the substitution $l_T/l_C=\lambda$, we can determine the matrix elements of the compliance tensor, $\mathbf{C}^{-1}$, and the stiffness tensor, $\mathbf{C}$, of the "ideal cantilever" in the flat coordinate system YZ, see also [14]:

$$\mathbf{r^C}=\mathbf{C}^{-1}\mathbf{F},\quad \mathbf{C}^{-1}=k_C^{-1}\begin{pmatrix}3\lambda^2 & 3\lambda/2\\ 3\lambda/2 & 1\end{pmatrix},\tag{4a}$$

$$\mathbf{F}{=}\mathbf{C}\mathbf{r}^{\mathbf{C}},\quad \mathbf{C}{=}k_C\begin{pmatrix}4/3\lambda^2 & -2/\lambda\\ -2/\lambda & 4\end{pmatrix}. \tag{4b}$$

Using (4a) in (2a) and (2b), we can relate the bending angle and the displacement of the console measured by the OBD and interferometer methods with the probe tip displacements:

$$\alpha\left(\psi,\mathbf{r}^{\mathbf{C}}\right)=l_C^{-1}\left\{\psi\left(3\psi{-}2\right)Y^C/\lambda{+}6\psi\left(1{-}\psi\right)Z^C\right\}, \tag{5a}$$

$$Z\left(\psi,\mathbf{r}^{\mathbf{C}}\right)=\psi^2\left(\psi{-}1\right)Y^C/\lambda{+}\psi^2\left(3{-}2\psi\right)Z^C. \tag{5b}$$

Let the "ideal cantilever" be in contact with a flat, horizontal and non-deformable surface. If this surface is raised to a height of Z, the probe tip moves vertically by the same value, $Z^C{=}\,Z$. We can set the lateral displacement Y^C in two extreme cases: 1) the probe slides along the sample, $F_Y{=}\,0$ (according to (4a), this is equivalent to $Y^C{=}3\lambda Z^C/2$); 2) the probe is clamped on the sample, $Y^C{=}\,0$ ($F_Y{=}\,-F_Z/2\lambda$, according to (4b)), – and calculate using (5a) and (5b) the profiles of the console displacement and bending angle, see Table 1.

TABLE 1. "Ideal cantilever". Profiles of the console displacement and bending angle when the probe-sample contact moves to a height Z. The sample is horizontal, flat and non-deformable; the console is parallel to the sample

Contact	$Z\left(\psi\right)/Z$	$2l_C\alpha\left(\psi\right)/3Z$
Clamped ($Y^C=0$)	$\psi^2\left(3-2\psi\right)$	$4\psi\left(1-\psi\right)$
Sliding ($F_Y=0$)	$\psi^2\left(3-\psi\right)/2$	$\psi\left(2-\psi\right)$

Only when $\psi{=}1$, $Z\left(1\right)$ does not depend on Y^C. This point is the probe tip projection on the console plane, it may not coincide with the console edge. For the OBD method the special point is $\psi{=}2/3$, where $\alpha\left(\psi\right)$ depends only on Z^C. Since in AFM, the console deflection is regulated, for the "ideal cantilever" this point is optimal for OBD laser focusing. At $\psi{=}2/3$, in the controlled signal, the contribution from clamped state – sliding state transitions in the probe–sample contact (the main sources of instabilities during contact scanning) is suppressed, and the ratio $\alpha\left(\psi\right)/Z$, the sensitivity, is only $1/9$ less than the maximum. In AFM, the console is tilted from the horizontal line by a certain angle α_0. It can be shown that in this case the optimal focus will be almost at the same point: $\psi^*\cong 2\left(1{-}\lambda\tan^2\alpha_0+O\left(\lambda^2\right)\right)/3\cong 2/3$, since usually $\lambda\ll 1$.

In Fig. 2(b) the transverse force F_X twists the console at an angle β (measured by the OBD method) and additionally bends it and shifts its end by a distance $X^{C(b)}$. Such a bend leaves the console in the XY plane and it cannot be measured by the OBD or interferometer methods. By analogy with the F_Z component action considered in (2), we can write:

$$X^{C(b)}{=}\left(4l_C^3/E_Ctw^3\right)F_X{=}k_C^{-1}\delta^2F_X, \tag{4}$$

where $\delta{=}t/w$. The profile of the console torsion angle caused by the force moment F_Xl_T, responds to the relation, see details in [6,14]:

$$\beta\left(\psi,\mathbf{F}\right)=-\psi\left(3l_C/G_Cwt^3\right)F_Xl_T, \tag{6a}$$

where the console shear modulus $G_C{=}E_C/(2+2\nu)$. For most materials, the Poisson's ratio $\nu\approx 1/3$; using the notation introduced earlier, we transform (6a):

$$\beta\left(\psi,\mathbf{F}\right)=-\left(2/k_Cl_C\right)\lambda\psi F_X. \tag{2c}$$

The action of the force F_X gives a superposition of the torsion and the in-plane bending. Using (6) and (2c), the total displacement of the probe tip is obtained:

$$X^C{=}X^{C(b)}{-}l_T\beta\left(1{,}\mathbf{F}\right)=k_C^{-1}\left(2\lambda^2{+}\delta^2\right)F_X. \tag{6b}$$

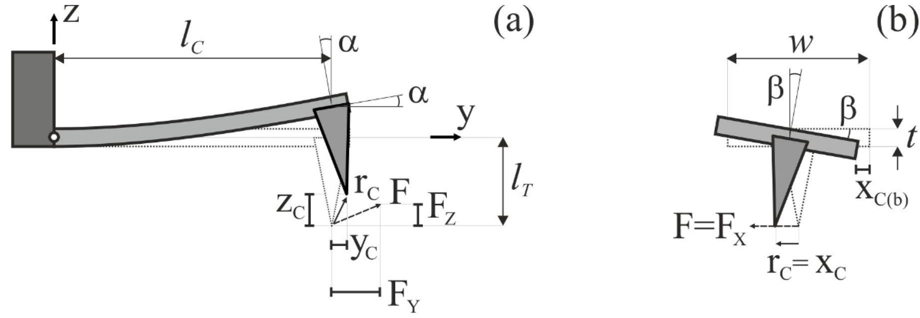

FIG. 2. "Ideal cantilever". (a) The console bending by the force $\mathbf{F}$ with components F_Y, F_Z. Both the free end of the console and the non-deformable probe are deflected by a positive angle α. As a result, the probe tip moves along the vector $\mathbf{r^C}$ with the components Y^C, Z^C. (b) Torsion by a negative angle β and bending of the console to a distance $X^{C(b)}$ by the force $\mathbf{F}$ with a single, positive component F_X. The probe tip shifts in the direction of the force along the vector $\mathbf{r^C}$ with the component X^C. The console width w, thickness t and length l_C; the probe height l_T; the Y and Z axes of the coordinate system associated with the cantilever

Using (6b), (4a), and (4b), we write the matrix elements of the compliance tensors, $\mathbf{C}^{-1}$, and the stiffness tensor, $\mathbf{C}$, of the "ideal cantilever" in the XYZ coordinate system:

$$\mathbf{C}^{-1}=k_C^{-1}\begin{pmatrix} 2\lambda^2+\delta^2 & 0 & 0 \\ 0 & 3\lambda^2 & 3\lambda/2 \\ 0 & 3\lambda/2 & 1 \end{pmatrix},$$

$$\mathbf{C}=k_C\begin{pmatrix} \left(2\lambda^2+\delta^2\right)^{-1} & 0 & 0 \\ 0 & 4\lambda^{-2}/3 & -2\lambda^{-1} \\ 0 & -2\lambda^{-1} & 4 \end{pmatrix}. \tag{4c}$$

Dividing (2c) by (6b), we relate the console torsion angle measured by the OBD method to the displacement:

$$\beta\left(\psi,\mathbf{r^C}\right)=-l_C^{-1}\lambda\psi X^C/\left(2\lambda^2+\delta^2\right). \tag{5c}$$

When the laser focus is fixed, $\psi=const$, the equations (5a) – (5c) can be used to restore the displacement vector of the ideal cantilever from the three measured parameters, and the equations (2a) – (2c) to restore the force vector,see Table 2. The necessary three parameters can be obtained both in the combined OBD and interferometer scheme [11, 12], and using only the OBD method and two ψ values. In contrast to the restored force vector, the restored $\mathbf{r^C}$ describes only the probe tip displacements of the "ideal cantilever".

TABLE 2. Profiles of the console vertical displacement, bending and torsion angles as functions of the displacement or of the force projections

Profile	$r^C=\left(X^C,Y^C,Z^C\right)$	$F=\left(F_X,F_Y,F_Z\right)$
$Z(\psi)$	$\psi^2(\psi-1)Y^C/\lambda+\psi^2(3-2\psi)Z^C$	$(1/2k_C)\left\{3\lambda\psi^2F_Y+\left(3\psi^2-\psi^3\right)F_Z\right\}$
$\alpha(\psi)$	$(1/l_C)\left\{\psi(3\psi-2)Y^C/\lambda+6\psi(1-\psi)Z^C\right\}$	$(3/2k_Cl_C)\left\{2\lambda\psi F_Y+\left(2\psi-\psi^2\right)F_Z\right\}$
$\beta(\psi)$	$-(2/l_C)\lambda\psi X^C/\left(2\lambda^2+\delta^2\right)$	$-(2/k_Cl_C)\lambda\psi F_X$

2.2. Deformation distribution in the console–probe–sample system

To calculate the profiles of the console displacements, bending and torsion angles for the "real cantilever", we consider the console–probe–sample system, see Fig. 3, and analyze how deformations are redistributed in it.

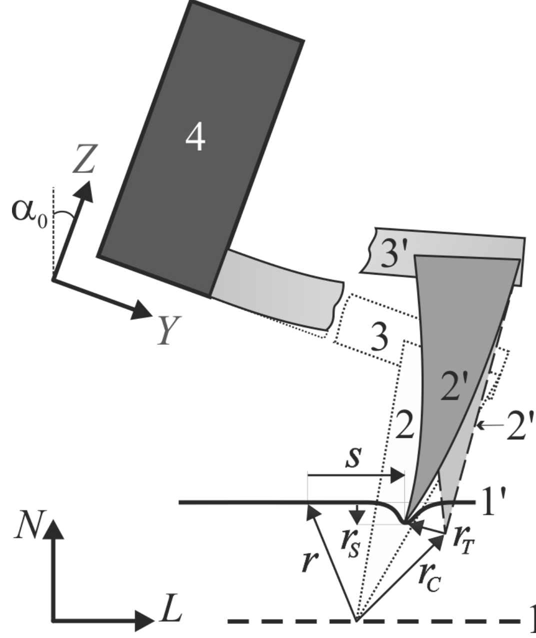

FIG. 3. Deformation of the sample and cantilever AFM in contact. Initial state: the sample (1) touches the probe (2), the interaction force is zero, the console (3) is not bent. Final state: the sample (1) moved along the vector $\mathbf{r}$, deforms itself, the probe (2) and the console (3); the non-deformable holder (4) is stationary, the conditionally non-deformable probe is in the position (2"). Deformation vectors of: ideal cantilever (the conditional probe tip (2") displacements), $\mathbf{r}^C$; probe tip, $\mathbf{r}^T$; sample, $\mathbf{r}^S$. The sliding is along the vector $\mathbf{s}$. The XLN coordinate system is associated with the scanner, XYZ – with the cantilever, the X axis is directed to the reader. The mounting angle of the cantilever holder, α_0, is deviated from the vertical: by 20° (NT-MDT microscopes) and by 12° (Bruker microscopes)

In each subsystem: console, "ideal cantilever", C, probe, T, sample, S, – the generalized Hooke's law is valid. Symmetric, positive definite stiffness tensors $C_{i,j}$, $T_{i,j}$, $S_{i,j}$ with nonzero determinants relate the force and associated vector components, $F_i^{C,T,S}$ and $r_j^{C,T,S}$, in the corresponding subsystem.E.g., for the "ideal cantilever": $F_i^{C,T,S}{=}C_{i,j}r_j^{C,T,S}$, see in Equation (4c) the matrix elements $C_{i,j}$ in the XYZ coordinate system. The quadratic forms of the tensors $\mathbf{C}$, $\mathbf{T}$, and $\mathbf{S}$ are expressions for the doubled elastic strain energy of the corresponding subsystem. The energy of the whole system is:

$$W{=}\frac{1}{2}\sum_{i,j}\left(C_{i,j}r_i^C r_j^C{+}T_{i,j}r_i^T r_j^T{+}S_{i,j}r_i^S r_j^S\right). \tag{5}$$

In the initial state $3/2/1$, Fig. 3, all coordinates are zero, there are no deformations, what minimizes the energy (7). When the sample holder moves along the vector $\mathbf{r}{=}\,(X,L,N)$ relative to the cantilever holder (this is done by the AFM scanner), then the deformation vectors appear in each subsystem: $\mathbf{r^C}{=}\,\left(X^C,Y^C,Z^C\right)$, $\mathbf{r^T}{=}\,\left(X^T,Y^T,Z^T\right)$ and $\mathbf{r^S}{=}\,\left(X^S,Y^S,Z^S\right)$. In the final equilibrium state $3'/2'/1'$, Fig. 3, the nine components of these vectors must be the coordinates of the conditional minimum of the energy.

Two cases are important, see also Fig. 3: a) the contact is clamped, $s\equiv 0$; b) the contact slides in some plane, $\mathbf{s}\neq 0$.

Case a). The system integrity is maintained, the deformation vectors obey the holonomic constraint:

$$\mathbf{r^C}{+}\mathbf{r^T}{-}\mathbf{r^S}{=}\mathbf{r}. \tag{7a}$$

The minimum energy is determined by zeroing the nine partial derivatives of W (7). Accounting for (7a), the minimum W is sought by solving a system of six equations for six unknown variables.

Case b). Let the contact slides in the XL plane, as in Fig. 3. Then the holonomic constraint will be only for the three vertical deformations:

$$N^C + N^T - N^S = N. \tag{7b}$$

The minimum W is sought by solving a system of eight equations for eight unknown variables.

Case a). According to the Newton's 3rd law, the forces $\mathbf{F^T}$ and $\mathbf{F^C}$, the action of the sample on the probe and the probe on the console, are equal to $-\mathbf{F^S}$, the counteraction of the probe on the sample. In each subsystem, the generalized Hooke's law is valid, e.g. $\mathbf{F^T}=\mathbf{Tr^T}$. This allows to relate the vectors $\mathbf{r^C}$, $\mathbf{r^T}$ and $\mathbf{r^S}$, and the vector $\mathbf{r}$:

$$\begin{cases} \mathbf{r^C}+\mathbf{r^T}-\mathbf{r^S}=\mathbf{r} \\ \mathbf{F^C}=\mathbf{F^T}=-\mathbf{F^S} \\ \mathbf{Cr^C}=\mathbf{Tr^T}=-\mathbf{Sr^S} \end{cases} \Rightarrow \begin{cases} \left(\mathbf{I}+\mathbf{T}^{-1}\mathbf{C}+\mathbf{S}^{-1}\mathbf{C}\right)\mathbf{r^C}=\mathbf{r} \\ \mathbf{r^T}=\mathbf{T}^{-1}\mathbf{Cr^C} \\ \mathbf{r^S}=-\mathbf{S}^{-1}\mathbf{Cr^C} \end{cases} \Rightarrow \begin{cases} \mathbf{r^C}=\mathbf{C}^{-1}\left(\mathbf{C}^{-1}+\mathbf{T}^{-1}+\mathbf{S}^{-1}\right)^{-1}\mathbf{r} \\ \mathbf{r^T}=\mathbf{T}^{-1}\left(\mathbf{C}^{-1}+\mathbf{T}^{-1}+\mathbf{S}^{-1}\right)^{-1}\mathbf{r} \\ \mathbf{r^S}=-\mathbf{S}^{-1}\left(\mathbf{C}^{-1}+\mathbf{T}^{-1}+\mathbf{S}^{-1}\right)^{-1}\mathbf{r} \end{cases} \tag{8a}$$

Where $\mathbf{I}$ is the unit matrix; $\mathbf{C}^{-1}$, $\mathbf{T}^{-1}$ and $\mathbf{S}^{-1}$ – the compliance (inverse stiffness) tensor of the corresponding subsystem. Unlike matrix elements, the solution form (8a) does not depend on the choice of the coordinate system. In the system, where the matrix elements of the tensors are the least bulky, calculations are simplified.

Case b). For the contact sliding in the XL plane, deformations of the "ideal cantilever" X^C, L^C, N^C, probe X^T, L^T, N^T, and sample X^S, L^S, N^S, will depend only on N, the vertical displacement of the scanner, although the latter moves the sample along the vector $\mathbf{r}=(X, L, N)$. We give this solution, omitting the cumbersome algebraic derivation:

$$\begin{pmatrix} X^C & X^T & X^S \\ L^C & L^T & Y^S \\ N^C & N^T & N^S \end{pmatrix} = \begin{pmatrix} C^{-1}_{NX} & T^{-1}_{NX} & -S^{-1}_{NX} \\ C^{-1}_{NL} & T^{-1}_{NL} & -S^{-1}_{NL} \\ C^{-1}_{NN} & T^{-1}_{NN} & -S^{-1}_{NN} \end{pmatrix} \frac{N}{C^{-1}_{NN}+T^{-1}_{NN}+S^{-1}_{NN}}, \tag{8b}$$

where e.g. C^{-1}_{NX} is the matrix element of the console compliance tensor in the XLN system associated with the scanner (or with the horizontally located flat sample), Fig. 3. The numerator in (8b) is proportional to N, the scanner displacement projection on the normal to the surface of sliding (the XL plane).

On the non-planar relief sample, the normal at the selected point on the sample may not coincide with the N axis. In this case, the local coordinate system xyz associated with the selected point is used, and the solution is obtained from (8b) by replacing: $X \to x,\ L \to y, N \to z$.

To calculate the bending and torsion angle profiles and the displacement profile, Table 2, the solution vector is taken in the coordinate system associated to the cantilever. For example in Fig. 3, the coordinate systems correspond to the following relation:

$$\begin{pmatrix} X^C \\ Y^C \\ Z^C \end{pmatrix} = \begin{pmatrix} 1 & 0 & 0 \\ 0 & \cos\alpha_0 & -\sin\alpha_0 \\ 0 & \sin\alpha_0 & \cos\alpha_0 \end{pmatrix} \begin{pmatrix} X^C \\ L^C \\ N^C \end{pmatrix}. \tag{9}$$

2.3. "Real cantilever"

An AFM pyramidal probe can be modeled by a truncated elliptical cone. In the cantilever coordinate system, both the stiffness and the compliance tensors of such a model have three components:

$$\mathbf{T}= \begin{pmatrix} k_{T1} & 0 & 0 \\ 0 & k_{T2} & 0 \\ 0 & 0 & k_{T3} \end{pmatrix}, \quad \mathbf{T}^{-1}= \begin{pmatrix} k^{-1}_{T1} & 0 & 0 \\ 0 & k^{-1}_{T2} & 0 \\ 0 & 0 & k^{-1}_{T3} \end{pmatrix}, \tag{10}$$

where k_{T1} and k_{T2} are the bending stiffness along the mutually perpendicular ellipse axes, k_{T3} is the normal stiffness along the cone height.

For a simplified model of a truncated cone with an apex radius R_T and the apex half angle α_T, it is sufficiently to determine two stiffness values, e.g. in the framework of theories of small deflections of rods [15, 16] and contact

mechanics [15, 17]:

$$k_{T1}{=}k_{T2}{=}k_{Tl} \cong (3\pi/4)\, E_T R_T (\tan\alpha_T\,)^3, \quad k_{T3}{=}k_{Tn} \cong 2E_T R_T. \tag{10a}$$

Si pyramidal probes e.g. on cantilevers HA_FM (NT–MDT SI) have the following parameters: Young's modulus: $E_T \approx 100$ GPa, $R_T \approx 10$ nm, $\alpha_T \approx 15°$. Using (10a) we get: $k_{Tl} \approx 50$ N/m, $k_{Tn} \approx 2000$ N/m.

For a more complex probe model, the truncated elliptical cone, let the semi axes of the ellipse lie along the X and Y directions, having dimensions c and d on the vertex. It can be shown that: $k_{T1}{=}q^{1/2}k_{Tl}$ and $k_{T2}{=}q^{5/2}k_{Tl}$, where the compression factor $q = d/c$, and the replacement $R_T{=}\sqrt{cd}$ is used in (10a) for k_{Tl} and k_{Tn}.

By analogy with the matrix elements (10), for the probe–sample contact we introduce the shear stiffness in the XLN coordinate system, $k_{S1}{=}k_{S2}{=}k_{Sl}$, and the normal stiffness, $k_{S3}{=}\,k_{Sn}$. Their values can be evaluated using the Hertz's contact mechanics, [17]:

$$\begin{gathered} k_{Sl}{=}\,8G^*a, \quad k_{Sn}{=}\,2E^*a{=}\sqrt[3]{6FR^*E^{*2}}, \\ a{=}\sqrt[3]{3FR^*/4E^*}, \quad R^*{=}R_TR_S/(R_T{+}R_S), \\ E^*{=}\left(\frac{1{-}\nu_T^2}{E_T}{+}\frac{1{-}\nu_S^2}{E_S}\right)^{-1}, \quad 4G^*{=}\left(\frac{(1{-}\nu_T/2)\,(1{+}\nu_T)}{E_T}{+}\frac{(1{-}\nu_S/2)\,(1{+}\nu_S)}{E_S}\right)^{-1}, \end{gathered} \tag{10b}$$

F – the interaction force, R_T and R_S – the tip curvature radius and the local curvature radius of the sample, E_T, ν_T and E_S, ν_S – Young's moduli and Poisson's ratios of the probe and sample, respectively.

Most materials have $\nu \approx 1/3$, therefore according (10b), $E^* \approx 4G^*$, and $k_{Sl} \approx k_{Sn}{=}k_S$. In this isotropic case, the sample local mechanical properties are modeled by one parameter k_S. Let both the probe with $R_T = 10$ nm and the flat, uniform sample be made of silicon, then for $F = 10$ nN we obtain: $k_S \approx 100$ N/m.

To use (8b), the tensor components of the sample, probe (10), console (4c) are converted using rotation matrices into values in the XLN coordinate system, see in particular (9). We give, for example, expressions for the components S^{-1}_{NN}, T^{-1}_{NN} and C^{-1}_{NN}:

$$\begin{aligned} C^{-1}_{NN} &= k_C^{-1}\left(3\lambda^2\sin^2\alpha_0 - 3\lambda\sin\alpha_0\cos\alpha_0 + \cos^2\alpha_0\,\right); \\ S^{-1}_{NN} &= k_C^{-1}\kappa_S^{-1}; \quad T^{-1}_{NN}{=}k_C^{-1}\left(\kappa_{T2}^{-1}\sin^2\alpha_0 + \kappa_{T3}^{-1}\cos^2\alpha_0\,\right). \end{aligned} \tag{11}$$

Here and further relative stiffness values are introduced: $\kappa_S{=}k_S/k_C$, $\kappa_{Ti}{=}k_{Ti}/k_C$, $i = 2, 3$.

To use (8a), we write $\mathbf{T}^{-1}{+}\mathbf{S}^{-1}$ by analogy with $\mathbf{T}^{-1}$ in (10), replacing k_{Ti}^{-1} with $k^{-1}\kappa_i^{-1}$, where $\kappa_i^{-1}{=}\kappa_{Ti}^{-1}{+}\kappa_S^{-1}$ and $i = 1, 2, 3$:

$$\mathbf{T}^{-1}{+}\mathbf{S}^{-1}{=}k_C^{-1}\begin{pmatrix} \kappa_1^{-1} & 0 & 0 \\ 0 & \kappa_2^{-1} & 0 \\ 0 & 0 & \kappa_3^{-1} \end{pmatrix}. \tag{12}$$

For the clamped contact, the proportionality coefficients between α or β and the displacement along the scanner selected axis can be obtained by substituting the matrix elements from (4c) and (12) into (8a), and using (9) and Table 2. For the sliding contact, to relate α and the scanner vertical displacement, one has to substitute in (8b) the matrix elements of the compliance tensors of the console, the sample, and the probe defined in the XLN coordinate system, see (11). Dependencies calculated in this way are shown in Table 3 as the normalized sensitivity profiles.

Using Table 3, we can significantly refine the equation (1). The ratio α/N is proportional to the force curve slope S; on the non-deformable sample ($\kappa_S^{-1}{=}\,0$) it is proportional to S_0. For the sliding contact, using the profile 1 from Table 3, we can compose analytical expressions for S and S_0 and obtain a new formula for k_S, which differs from the equation (1) by the correcting γ-factor:

$$\begin{aligned} \gamma &= \left(\left(3\lambda^2{+}\kappa_{T2}^{-1}\right)\sin^2\alpha_0 - 3\lambda\sin\alpha_0\cos\alpha_0 + \left(1{+}\kappa_{T3}^{-1}\right)\cos^2\alpha_0\,\right)^{-1}, \\ k_S &= \gamma k_C S/(S_0{-}S). \end{aligned} \tag{1a}$$

With growing k_C, the relative compliances κ_{T2}^{-1} and κ_{T3}^{-1} increase, and the γ-factor can become less than unity. The γ-factor of a soft cantilever (κ_{T2}^{-1} and κ_{T3}^{-1} are small) is larger than unit, e.g. for $\lambda{=}\,0.1$ and $\alpha_0{=}\,20°$ the soft cantilever has $\gamma \approx 1.27$. If the γ-factor is neglected, the k_S will be overestimated in the first case, and in the second one it will be underestimated.

Earlier [18] it was reported, when calibrating the AFM cantilever stiffness the result is overestimated, in proportion $\cos^{-2}\alpha_0$ [19]. The expression (1a) for γ-factor substantially clarifies these remarks.

TABLE 3. "Real cantilever" in contact with the horizontal, deformable sample surface. Normalized profiles of the console bending and torsion angles (α and β) as functions of the scanner displacements (X, L, N)

No.	Normalized sensitivity profile
1	$\frac{2l_C\alpha_{b)}(\psi)}{3N}=\frac{(2-\psi)\cos\alpha_0-2\lambda\sin\alpha_0}{\left(3\lambda^2+\kappa_2^{-1}\right)\sin^2\alpha_0-3\lambda\sin\alpha_0\cos\alpha_0+\left(1+\kappa_3^{-1}\right)\cos^2\alpha_0}\psi$
2	$\frac{2l\alpha_{a)}(\psi)}{3N}=\frac{\left(4+4\kappa_3^{-1}\right)\lambda\sin\alpha_0+\left(12\lambda^2+8\kappa_2^{-1}\right)\cos\alpha_0-\left[6\lambda\sin\alpha_0+\left(12\lambda^2+4\kappa_2^{-1}\right)\cos\alpha_0\right]\psi}{3\lambda^2+12\lambda^2\kappa_3^{-1}+4\kappa_2^{-1}+4\kappa_2^{-1}\kappa_3^{-1}}\psi$
3	$\frac{2l\alpha_{a)}(\psi)}{3L}=\frac{\left(-4+8\kappa_3^{-1}\right)\lambda\cos\alpha_0+\left(12\lambda^2+8\kappa_2^{-1}\right)\sin\alpha_0+\left[6\lambda\cos\alpha_0-\left(12\lambda^2+4\kappa_2^{-1}\right)\sin\alpha_0\right]\psi}{3\lambda^2+12\lambda^2\kappa_3^{-1}+4\kappa_2^{-1}+4\kappa_2^{-1}\kappa_3^{-1}}\psi$
4	$\frac{2l\beta_{a)}(\psi)}{3X}=\frac{-4\lambda}{6\lambda^2+3\delta^2+3\kappa_1^{-1}}\psi$

Subscripts a) and b) refer to the clamped and sliding contacts. Relative compliances $\kappa_i^{-1}=\kappa_{Ti}^{-1}+\kappa_S^{-1}$, $i=1,2,3$ correspond to X,Y,Z axes. Mounting angle of the cantilever holder α_0; $\lambda=l_T/l_C$, $\delta=t/w$; see Fig. 2 and 3. At the line of the console attachment to the chip $\psi=0$, at the point of the probe tip projection to the console plane $\psi=1$.

If the probe–sample contact is clamped when calculating at least one of the slopes, S or S_0, the expression defining the k_S is significantly complicated, in particular by the dependence on ψ.

In this regard, it is important to determine in AFM whether the probe slides along the sample or not. E.g. for a homogeneous sample, the sliding probe should as a rule lead to reduced S values on the inclined surface areas compared to the horizontal ones [20]. In detail, using the analytical approach of this work, the question will be considered later.

When substituting $\kappa_i^{-1}=0$, the profiles in Table 3 describe the "ideal cantilever" on the non-deformable and horizontal sample. A special case when the console is parallel to the sample ($\alpha_0=0$) was considered in Table 1. The estimations made above for the probe and sample stiffness values may be used to conclude the following: 1) $\kappa_1^{-1}\cong\kappa_2^{-1}\gg\kappa_3^{-1}$, 2) $\kappa_i^{-1}\ll 1$ for soft cantilevers ($k_C<1N/m$). Thus on the solid and flat sample, the soft cantilevers should behave like the "ideal cantilever", some deviations from this behavior can be described using two small parameters, κ_1^{-1} and κ_2^{-1}.

3. Experimental verification of the theory and the results discussion

For the OBD method used in our AFM device, the console bending angle α is proportional to the DFL(deflection) signal, the photocurrent difference between the upper and lower halves of the photodetector; the console torsion angle β is proportional to the LF (lateral force) signal, the photocurrent difference between the right and left halves of the photodetector, [13]. The ratios α/N, α/L and β/X as functions of ψ were measured by analyzing the force dependencies $DFL(N)$ and the friction force loops $DFL(L)$ and $LF(X)$. In these measurements, an atomically smooth, freshly prepared n-type GaAs (110) cleaved surface (a doping level is 10^{18} cm^{-3}) was used as a flat and solid sample.

DFL and LF signals are measured in Amps or Volts, depending on the AFM model. To compare the measurement results with the calculations, it is necessary to convert the used units into radians.We use the AFM device Ntegra Aura (NT–MDT SI) in the configuration "scanning by sample". The screws that adjust the horizontal position of the photodetector along and across the console have a thread pitch of 0.35 mm. The angular size of the vector of the photodetector center displacement is inversely proportional to the optical arm, 25 mm. The light reflected in the photodetector is deflected by a double angle compared to the console deflection angle [21]. Given this and that

in our AFM device the photodetector and console planes are parallel, one turn of the adjusting screw along the console corresponds to α=cos $20° \cdot 0.35\ /50 \cong 6.6 \cdot 10^{-3}$ rad, and one turn of the adjusting screw across the console to β=$0.35/50 = 7 \cdot 10^{-3}$ rad. This made it possible to quickly measure the necessary conversion factors for DFL and LF signals with an accuracy of about 5 % (1/24 turn).

Measurements of ψ, the focus point position of the OBD laser on the console, were carried out using the adjusting screw (0.35 mm thread pitch) moving a micropositioner table with the cantilever holder along the console. Given the length ($\approx$ 51 mm) of the lever of the force acting on the table, and the distance ($\approx$ 34 mm) from the cantilever to the table axis of rotation, one turn of the screw corresponds to the movement of $\approx$ 233 μm. Using this, it was possible to change the focus point position with an accuracy of about 10 μm (1/24 turn). The positions of the console attachment to the chip and of the free end of the console were determined by a 50 % reduction in the intensity of laser radiation reflected from the console to all four sections of the photodetector (a *Laser* signal).

Figure 4 presents the results of AFM measurements of the console bending and torsion angles caused by the movements of the GaAs (110) sample in three orthogonal directions. The cantilever fpS10 [22] with the following characteristics was studied. The console stiffness refined by the Sader method [23] was k_C= 51 mN/m. The geometric parameters of the console and probe, refined in an optical and scanning electron microscopes: l_C= 257 μm (the distance between the line of the console attachment to the chip and the point of the probe tip projection to the console plane), w = 34 μm and t = 1 μm; α_T= 10.5° and l_T= 12.5 μm.

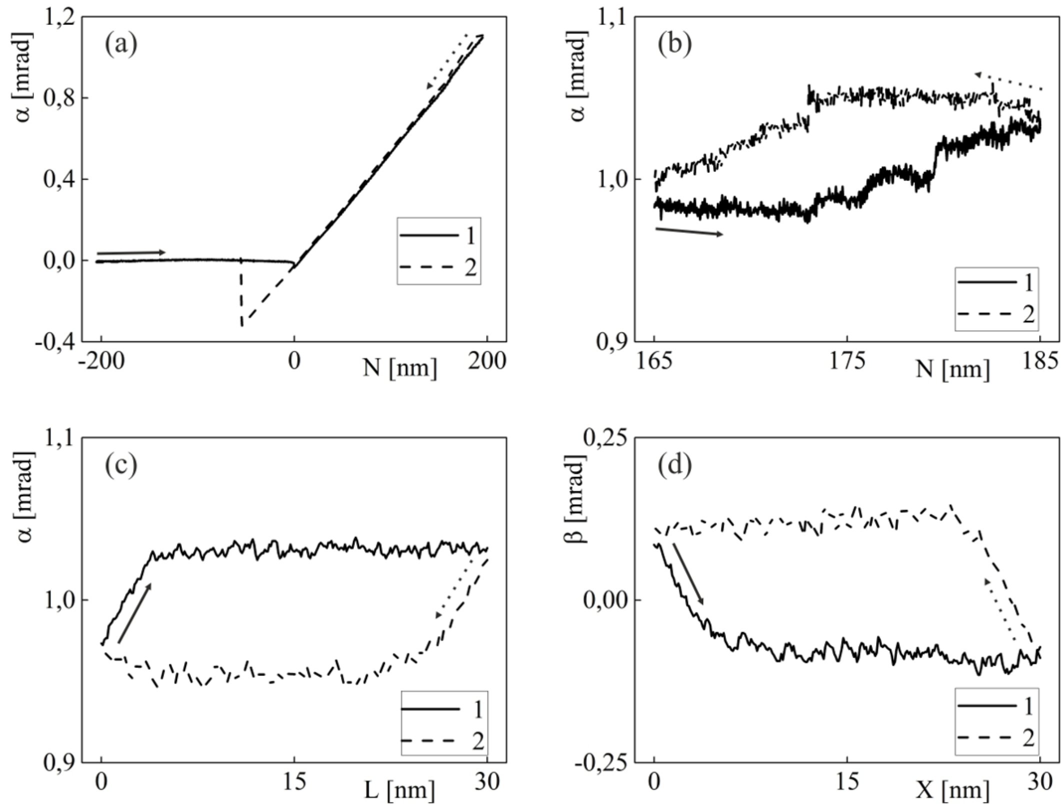

FIG. 4. (a) Force curves, $\alpha(N)$, DFL signal dependencies on the scanner vertical displacement: 1 loading; 2 unloading. Friction loops (hysteresis): (b) $\alpha(N)$, in the force curves; (c) $\alpha(L)$, in the DFL signal, the fast scanning direction is along the console; (d) $\beta(X)$, in the LF signal, the fast scanning direction is across the console. The scanning velocities both in positive 1 and negative 2 directions were: (a) 200 nm/s, (b) 10 nm/s, (c) and (d) 60 nm/s. (b–d) The interaction force, $F \approx 10$ nN. The OBD laser focus point coordinate on the console, $\psi = 0.95$

The experimental α/N ratio was determined for positive N as the average slope of the loading and unloading force curves. In particular it is 5.87 μrad/nm for the data in Fig. 4(a). The ratios α/L and β/X were determined on the left and right sides of the friction loops [18, 24], see arrows in Figs. 4(c) and 4(d) along the areas where the probe tip is clamped by the sample. To improve the accuracy of measurements, 32 friction loops were analyzed.

Using the data, as in Fig. 4, with different ψ, the profiles of the console torsion, buckling and bending angles were measured, see Fig. 5.

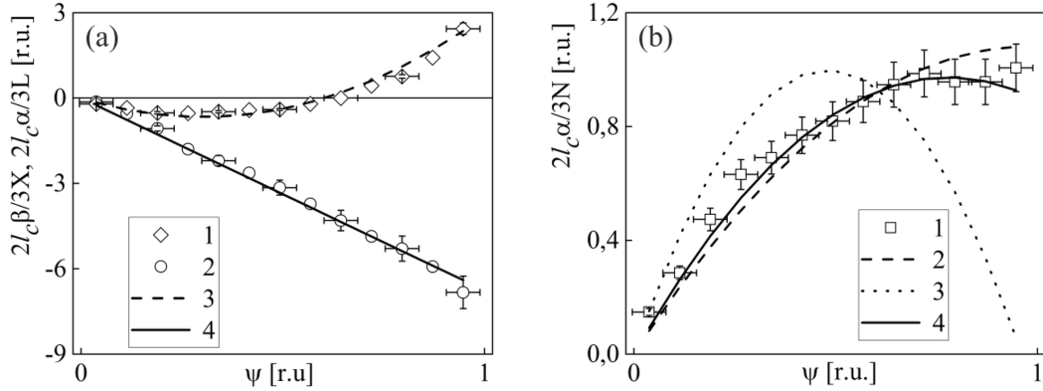

FIG. 5. Cantilever fpS10. (a) Measurement and approximation data for the buckling angle profile, 1 and 3, and torsion angle, 2 and 4, of the console. Model curves 3 and 4 are calculated according to the analytical dependencies 3 and 4 of Table 3 with the parameters, respectively: $k_2^{-1} = 0.007$ and $k_3^{-1} = 0$; $k_1^{-1} = 0.004$. (b) Measurement 1 and approximation 2–4 data for the bending angle profile of the console. Model curves 2 and 3 correspond to the dependencies 1 and 2 of Table 3 with the parameters $k_2^{-1} = 0.007$ and $k_3^{-1} = 0$. The curve 4 data are the sum of the 2 and 3 model profiles data with weights of 0.85 and 0.15

Measured torsion angle profile, Fig. 5(a), is well described by the ψ linear relationship 4 of Table 3 with a single fitting parameter $\kappa_1^{-1}= 0.004$. The fitting parameter value, see the discussion of expressions (10) and (11), corresponds to the bending stiffness of the probe $k_{T1} \cong 12.75$ N/m. Using (10a), we can estimate the tip radius $R_{T1} \cong 8.5$ nm, that is consistent with the supplier information [19].

At the console edge, the buckling angle in Fig. 5(a) is positive, and closer to the console fixing line on the chip it is negative. A zero angle value and, as a consequence, the disappearance of the friction loop were observed at $\psi = 0.64$; at lower ψ, the friction loop was inverted. In Fig. 4(d), the signal 1 (2) first decreases (increases), and then goes horizontally; after inversion, the signal 1 (2) first increased (decreased) and then saturated. In Fig. 5(a) the measured profile is consistent with the dependence 3 of Table 3 with a single fitting parameter $\kappa_2^{-1}= 0.007$, whence using (10a) we get: $k_{T2} \cong 7.3$ N/m and $R_{T2} \cong 5$ nm. The value $\kappa_2\kappa_1^{-1}$ differs from unity and corresponds to the probe vertex ellipticity, compression factor $q = \sqrt{4/7} \cong 0.76$.

The friction loop, hysteresis, is also observed in the force curves, i.e. in the bending angle signal, Fig. 4(b). In contrast to Fig. 4(c) and 4(d), the signal, associated with the probe–sample clamping, goes almost horizontally.The disappearance and subsequent inversion of the friction loop in the force curves were detected at the same values, $\psi \leq 0.64$, as for the buckling angle signal in Fig. 4(c). This observation directly shows the contribution of the clamped state of the contact to the console bending angle value.

The fitting parameter $\kappa_2^{-1}= 0.007$ of the data in Fig. 5(a) was used to calculate the normalized sensitivity profiles for bending angle in cases of sliding and clamped contacts, dashed, 2, and dotted, 3, curves, Fig. 5(b). The experiment is better described by the sliding contact model. However, for $\psi \leq 0.64$ this model underestimates somewhat, and for $\psi \geq 0.64$ it overestimates the experiment. The best agreement with the experiment shows the combined model (the sliding and clamped contacts profiles with corresponding contributions of 0.85 and 0.15), a solid curve in Fig. 5(b).

Note that when $\kappa_i^{-1}= 0$ the difference between dependencies 1 and 2 in Table 3 is maximum. When the variable ψ is close to unity, the clamped contact leads to a significantly decreasing slope of the force curve in comparison with the sliding contact, see also Fig. 5(b). As a consequence, in the first case, the sample may appear softer in the AFM measurement than in the second one. In this regard, simple experimental criteria are very important in distinguishing the sliding contact from the clamped one.

Thus, for the studied soft ($k_C \ll 1$ N/m) contact cantilever, all the three measured profiles agree well with the calculations. In each case, the fitting procedure used only one parameter. It turned out that $\kappa_2^{-1} \ll 1$, and the parameter κ_3^{-1} was not required.

The calculations were also consistent with measurements performed on stiff ($k_C \gg 1$ N/m) cantilevers: NSG11 and HA_NC (NT–MDT SI), RTESP-150 (Bruker). The fitting parameters κ_1^{-1} and κ_2^{-1} increased, and κ_3^{-1} was also

used. It was found that the probes on these cantilevers are characterized by k_{Tl}~10 N/m, which is close to the result for the fpS10 cantilever.

We define the values k_C for which the γ-factor in (1a) is less than unity. Assuming that κ_{T3}^{-1} and λ^2 are small and therefore neglecting them, we have the following condition: $k_C > k_{T2}(1+3\lambda\cot\alpha_0)$. Taking for estimation $k_{T2}=k_{Tl}=10$ N/m and $\lambda=1/10$, for the mounting angle of the cantilever holder $\alpha_0=12°$, we get: $k_C>24$ N/m. The RTESP-300 cantilever (Bruker) has $k_C=40$ N/m; when neglecting the γ-factor the AFM overestimate k_S by 7 %. In the case of RTESP-525, $k_C=200$ N/m, k_S is overestimated by 75 % (and more than three times if $\alpha_0=20°$).

Unlike the soft cantilever, no friction loops were observed in the force curves measured with the stiff cantilevers. This is due to both the force sensitivity decrease and the diminishing difference between the normalized sensitivity profiles of the sliding and clamped contacts (1 and 2 in Table 3) with increasing κ_2^{-1} and κ_3^{-1}. To illustrate this, it is enough to consider the case of a very soft sample, when $\kappa_S^{-1} \gg 1$. Since then $\kappa_i^{-1} \cong \kappa_S^{-1}$, it can be shown that with growing κ_S^{-1} the dependence 1 converges to $\psi\,[(2-\psi)\cos\alpha_0 - 2\lambda\sin\alpha_0]\,\kappa_S$ and the dependence 2, to $\psi\,[(2-\psi)\cos\alpha_0 + \lambda\sin\alpha_0]\,\kappa_S$. Since λ is small, both limits are very close to: $\psi\,(2-\psi)\,\kappa_S\cos\alpha_0$.

4. Conclusion

The results of modeling the contact static interaction of the AFM cantilever with the sample are presented. An analytical model was created to calculate the distribution of deformation between the sample, the probe and the console. The model takes into account the following factors: the probe is clamped by the sample or slides along its surface, the geometric and mechanical characteristics of the sample and cantilever and their relative orientation. A new expression is proposed to determine the probe–sample stiffness. The expression that differs from the generally accepted one by a correction factor is proven to be used when the probe–sample contact is sliding. Normalized sensitivity profiles were simulated for the console bending and torsion angles as functions of three dimensional displacements of the mechanically isotropic sample.The profiles were also measured using AFM. Good agreement between measured and simulated data is demonstrated.

It is interesting to adapt the analytical model of this work to increase the accuracy of AFM studies of mechanically anisotropic samples, for example, when measuring the Young's modulus of suspended nanometer scale objects [25]. It is also important to extend the results of this work to ways for proving the sliding of the AFM probe along the sample when measuring force curves.

Acknowledgements

The author thanks his colleagues, Dr. M. M. Khalisov and Dr. A. A. Krasilin for constructive criticism of the manuscript.

Thus work is financially supported by the Russian Scientific Foundation, grant No. 19-13-00151.

References

[1] Binnig G., Quate C.F., Gerber Ch. Atomic Force Microscope. *Physical Review Letters*, 1986, **56** (9), P. 930–933.

[2] Scanning probe based apparatus and methods for low-force profiling of sample surfaces and detection and mapping of local mechanical and electromagnetic properties in non-resonant oscillatory mode. Patent Number: US 9,110,092 B1, USA. Date of Patent: Aug. 18, 2015. Int. Cl.: GOIN I3/6 (2006.01), G0IB 5/28 (2006.01). Inventors: Magonov S., Belikov S., Alexander J.D., Wall C.G., Leesment S., and Bykov V. Assignee: NT-MDT Development Inc., Tempe, AZ (US). Appl. No.: 14/247,041. Filed: Apr. 7, 2014. 10 Claims, 34 Drawing Sheets.

[3] Jumping probe microscope. Patent Number: 5,229,606, USA. Date of Patent: Jul. 20, 1993. Int. Cl.: H01J 37/26. Inventors: Elings V., Gurley J. Assignee: Digital Instruments, Inc., Santa Barbara, Calif. Appl. No.: 361,545. Filed: Jun. 5, 1989. 30 Claims, 4 Drawing Sheets.

[4] de Pablo P.J., Colchero J., Gomez-Herrero J., and Baro A.M. Jumping mode scanning force microscopy. *Applied Physics Letters*, 1998, **73** (22), P. 3300–3302.

[5] Kalinin A.S. PhD thesis. National Research Center "Kurchatov Institute", Moscow, 2017, 102 p.

[6] Sarid D. *Exploring scanning probe microscopy with MATHEMATICA*. 2nd ed. Weinheim: WILEY-VCH Verlag, 2007, 310 p.

[7] Ankudinov A.V., Khalisov M.M., et al. The Probe Length Effect on the Cantilever of an Atomic Force Microscope in Measuring the Mechanical Properties of Living Neurons. *Tech. Phys. Lett.*, 2018, **44** (8), P. 671–674.

[8] Alexander S., Hellemans L., et al. An atomicresolution atomicforce microscope implemented using an optical lever. *J. of Appl. Phys.*, 1989, **65** (1), P. 164–167.

[9] Fujisawa S., Ohta M., et al. Difference between the forces measured by an optical lever deflection and by an optical interferometer in an atomic force microscope. *Rev. Sci. Instrum*, 1994, **65** (3), P. 644–647.

[10] Kawakatsu H., Bleuler H., Saito T., Hiroshi K. Dual Optical Levers for Atomic Force Microscopy. *Jpn. J. Appl. Phys.*, 1995, **34**, 1 (6B), P. 3400–3402.

[11] Asylum Research Quantifies the "Last Axis" in Atomic Force Microscopy, 2018, URL: https://www.oxford-instruments.com.

[12] Labuda A., Proksch R. Quantitative measurements of electromechanical response with a combined optical beam and interferometric atomic force microscope. *Appl. Phys. Lett.*, 2015, **106** (25), 253103.

[13] Mironov V.L. *Fundamentals of the Scanning Probe Microscopy*. The Russian Academy of Sciences Institute of Physics of Microsructures, Nizhniy Novgorod, 2004, 97 p.

[14] URL: https://www.ntmdt-si.ru/resources/spm-theory/theoretical-background-of-spm.

[15] Landau L.D., Lifshitz E.M. *Theory of Elasticity*. Oxford, Pergamon Press Ltd., 1970, 177 p.

[16] Dunaevskiy M., Geydt P., et al. Youngs Modulus of Wurtzite and Zinc Blende InP Nanowires. *Nano Letters*, 2017, **17** (6), P. 3441–3446.

[17] Popov V.L., Heß M., Willert E. Handbook of Contact Mechanics. Exact Solutions of Axisymmetric Contact Problems, 2019. Translation from the German Language edition: Popov et al: Handbuch der Kontaktmechanik. Springer-Verlag GmbH Deutschland, 2018, 347 p.

[18] Heim L.-O., Kappl M., Butt H.-J. Tilt of Atomic Force Microscope Cantilevers: Effect on Spring Constant and Adhesion Measurements. *Langmuir*, 2004, **20**, P. 2760–2764.

[19] Hutter J.L. Comment on Tilt of Atomic Force Microscope Cantilevers: Effect on Spring Constant and Adhesion Measurements. *Langmuir*, 2005, **21**, P. 2630–2632.

[20] Timoshchuk K.I., Khalisov M.M., et al. Mechanical characteristics of intact fibroblasts studied by atomic force microscopy. *Tech. Phys. Lett.*, 2019, **45** (9), P. 947–950.

[21] Bhushan B. (Ed.) *Nanotribology and Nanomechanics. An Introduction*. Springer-Verlag, Berlin, Heidelberg, 2005, 1148 p.

[22] URL: http://nanoprobes.aist-nt.com.

[23] Sader J.E., Chon J.W.M., Mulvaney P. Calibration of rectangular atomic force microscope cantilever. *Rev. Sci. Instrum.*, 1999, **70**, P. 3967–3969.

[24] Mate C.M., McClelland G.M., Erlandsson R., Chiang S. Atomic-scale friction of a tungsten tip on a graphite surface. *Phys. Rev. Lett.*, 1987, **59**, P. 1942–1945.

[25] Salvetat J.-P., Briggs G.A.D., et al. Elastic and Shear Moduli of Single-Walled Carbon Nanotube Ropes. *Phys. Rev. Lett.*, 1999, **82**, P. 944–947.